Chapter 5: Conclusions and Future Directions

5.1 General Conclusions

The main objectives of this dissertation were to examine how small molecules and peptides can be used to study amyloid proteins, specifically Aβ and hIAPP. Recent developments have focused on the design and utilization of molecules that are capable of metal chelation and Aβ interaction (Chapter 2). Bifunctional compounds have been generated based on two rational structure-based design principles: linkage and incorporation. Our group has made significant progress in the formation of bifunctional molecules based on the incorporation approach, which have shown positive results in the ability to modulate the interaction/reactivity of metal-Aβ species to different extents. Utilizing several structural scaffolds of Aβ imaging agent frameworks or natural products we have created a family of compounds that can interact with metal-Aβ species and give valuable insights into their reactivity.

The work presented herein has elucidated a organic scaffold that can be used to perturb the interactions between metal ions and Aβ (Chapter 2). Though our **DPP** compounds displayed toxicity at low concentrations, the framework proves to be useful and can undergo further modifications in order to be optimized. These small molecules are useful due to their inherent bifunctionality and ability to modulate metal-associated Aβ aggregation differently than metal-free Aβ aggregation. A follow up study has modified the **DPP** framework and differences in reactivity with metal-Aβ has been seen. The planarity in the propynone moiety has provided to be beneficial for inhibiting and depolymerizing aggregate formation, but removal of this Michael acceptor functionality has greatly reduced cytotoxicity. Modifying this parent scaffold by tuning

the metal binding and Aβ interacting moieties will allow for developing ligands with the ideal properities for modifying metal-induced Aβ aggregates while keeping cell toxicity low.

Furthremore, Natural products have shown some promise against hIAPP aggregation and hIAPP-induced toxicity but there is still much to be done and many fundamental questions remain unanswered. Before much progress can be made, it is essential to know the actual dominant mechanism of toxicity by hIAPP. It is also essential that methods can be developed for high throughput screening for potential lead compounds. Most of these assays currently select against fiber inhibition with the assumption that stopping fiber formation will stop hIAPP toxicity. Natural products often exhibit antioxidative properties that may reduce ROS and may open up a new potential avenue for treatment. In Chapter 3, a newly developed curcumin analog, **CurDAc**, has shown promising activity against hIAPP in solution and in the presence of membrane lipids. The need for small molecules to mitigate and modify hIAPP aggregation is necessary due to their role in disease; however, due to the lack of structural targets it is become increasingly difficult to produce compounds which are effective. Using natural products as a foundation is valuable since nature has already optimized structural motifs for specific purposes (e.g. antioxidant, anti-inflammatory, anti-amyloidogenic). Curcumin, though has much application, has low stability and solubility in physiological conditions. **CurDAc** is a structural modification which has increased the stability of the molecule, as well as increased its solubility in aqueous conditions thus making it an ideal candidate to study against hIAPP aggregation. In Chapter 3, we have shown that this molecule inhibits hIAPP fibril formation at the membrane surface, depolymerizes preformed aggregates, and most interestingly, locks the peptide in a helical conformation. These properties can also be exploited to study the structure of hIAPP in solution using high-resolution techniques, such as NMR.

Fibrillization of hIAPP can be affected by many factors. Specifically, oligomeric structures within the membrane can act as largely non-selective ion channels and disrupt membrane permeability and misregulate metal ion homeostasis. However, other studies have shown the direct disruption of the membrane by the uptake of lipid molecules during fibrillogenesis into protofibril units. Membranes can therefore indirectly contribute to the cytotoxicity of IAPP by accelerating the formation of these toxic species. Although there is much evidence for mechanisms by which hIAPP aggregates cause cytotoxicity, it is becoming crucial to identify the (toxic) intermediates along the amyloid pathway. These intermediates comprise of various structures and the role of these species in fibrillation process has been the subject of much debate. Therefore, it is critical to study and understand the early stages of fibril assembly. Since amyloid proteins aggregate and produce heterogeneous species in solution, they are increasingly difficult to study. Therefore, small peptides, as presented herein (Chapter 4), have been be used as model systems to probe the kinetics and structural changes of amyloid aggregation in vitro. We have shown that **TK9** and its variants adopt fibril morphology after incubation, similar to that seen by Aβ and hIAPP. The association process of **TK9** seems to behave similarly to that of the self-associating regions of amyloid proteins, but at a slower time scale, making it ideal to study amyloid aggregation mechanism and kinetics. This short peptide was also able to inhibit hIAPP fibril formation, dose dependently, possibly making systems as such viable candidates for amyloid aggregation modulators, like small molecules.

5.2 Future Directions

In vitro biochemical and biophysical assays have provided a basis for more clearly understanding how small molecule natural products influence hIAPP aggregation and toxicity. Recently, mass spectrometry has been employed to give more detailed information about specific

interactions between these molecules and their peptide target; however to probe these interactions further, atomic-level resolution techniques need to be utilized. The screening of natural products using high-resolution NMR methods has not yet been used for studying hIAPP, but has demonstrated to be effective for other amyloid proteins. Measuring peak intensities and broadening through simple 1D NMR experiments can provide valuable information about the effect of ligands on hIAPP. Furthermore, STD NMR experiments have been used as a method for monitoring the contacts between specific atoms of a ligand and a larger protein target, like amyloid-β. Small molecules can also be screened against amyloid proteins using two-dimensional techniques, such as Heteronuclear Multiple Quantum Coherence (HMQC). Using these techniques it is possible to directly obtain residue specific information of ligand interactions with the peptide using a fast data acquisition approach (SOFAST), which can circumvent the possible changes in chemical shifts associated with peptide aggregation rather than ligand binding. Solid-state NMR methods can also be employed to investigate structural features related to small molecule interactions with amyloids when inaccessible to solution techniques, as seen with Aβ and EGCG and curcumin and resveratrol. Overall, NMR can be an effective tool to study the interactions between natural products and hIAPP, providing atomic-level details unobtainable by other techniques which can help elucidate mechanisms of inhibition or oligomer formation and stabilization.

The misfolding and subsequent aggregation of amyloidogenic proteins is a common pathological feature across a wide variety of diseases, including Alzheimer's disease (AD), Parkinson's disease and type II diabetes (T2D). A variety of peptides and proteins are known to proceed along a conserved nucleation dependent aggregation pathway despite minimal sequence homology. These peptides and proteins propagate to form amyloid species of various size,

morphology and toxicity and despite this ubiquitous misfolding pathway, the aggregation of amyloids remains difficult to modulate, redirect and control with chemical modulators with therapeutic potential. Efforts toward the identification of novel inhibitors and modulators of amyloid aggregation have been made; however, there has been no success in clinical trials to date. It is believed that shortcomings are due, in part, to a lack of a thorough understanding of any structure activity relationship (SAR) between small molecules and their ability to redirect the folding of amyloidogenic peptides/proteins. While high throughput screens are traditionally used to identify leads in small molecule-protein interactions, the lack of sequence homology between amyloidogenic species, as well as their poorly defined and intrinsically disordered structures in the monomeric and oligomeric states, makes traditional screens limited. To date, scientists have had to rely primarily on more laborious and low throughput methods such fluorescence, cell viability or microscopy studies to identify chemical modulators. A recent report has utilized mass spectrometry as a method to rapidly screen, define specific or non-specific binding to amyloid assemblies and measure shifts in monomer populations of amyloid peptides, which is the first account of high resolution analytical techniques to screen small molecules as amyloid aggregation modulators.

Future goals for this project are to apply a recently reported high throughput screening methodology specific for amyloids to identify small molecules capable of modulating the aggregation of both Aβ, implicated in AD and human islet amyloid polypeptide (hIAPP) associated with T2D. This screen will help identify compounds which specifically modulate the aggregation of Aβ and hIAPP independently, while also identifying ligands which modulate the aggregation activity of both peptides thus providing leads which can be used to modify aggregation of more than one amyloid protein. Compounds in each of these three categories

which can completely inhibit aggregation, speed up or slow down aggregation and increase or decrease aggregation will then be selected for in depth analysis through biophysical characterization and high resolution nuclear magnetic resonance experiments in order to elucidate 1. Structural motifs responsible for modulation, 2. Specific or non-specific interactions with the peptides 3. Structural characterization of amyloid species induced by the small molecule ligands and 4. Mechanism of action. These compounds can also be translated to cell-based assays, specifically cytotoxicity assays or through the application of reprogramming patient somatic cells. This method offers tremendous promise for studying how both internal factors (i.e., gene mutations), as well as external factors (i.e., small molecules) influence disease pathology and physiology. Patient-derived induced pluripotent stem cells (iPSCs) can be differentiated into disease-relevant cell types that were previously unavailable, such as motor neurons, cortical neurons or pancreatic cells that reflects the genetic background of that patient with AD or T2D. iPSCs mimicking the phenotypes of diseased individuals, could help identify in vitro defects in these cells that could reflect the underlying pathology of AD and T2D. Eventually, this work can be carried out into transgenic living models to asses the influence of the small molecules and peptides on animals to see how they behave in a more relevant biological setting.

Moreover, understanding the underlying mechanisms of amyloid formation are critical to studying their formation and toxicity. To track the transient formation of small oligomers of hIAPP, accelerated versions of the traditional HMQC and TROSY techniques (SOFAST-HMQC and BEST-TROSY) can be used to acquire real-time 2D NMR spectra in ~ 5 minutes compared to >60 minutes for a conventional spectrum. In an earlier study, diffusion based NMR experiments were used to show that IAPP does not form a stable population of small oligomers;

however, the limited time-resolution of these experiments prevented a direct detection of transient oligomers. Using the SOFAST-HMQC technique, transient oligomer formation is readily detectable during the lag-phase of aggregation (approximately the first 200 minutes), which will also help identify targets for therapeutic application.

Appendix A. Supporting Information for Chapter 2

Table A.1. Raw MS signal intensity data for the interaction of **DPP1** or **DPP2** with Aβ species

	DPP1					
	Avg Unbound Signal	*Avg Bound Signal*	*Total Signal for Bound/Unbound*	*% Bound*	*% ThT Bound*	*Normalized % Bound*
Monomer	20966.82	4336.01	25302.84	17.14	0.26	16.88
Dimer	2527.24	1386.40	3913.64	35.42	0.00	35.42
Trimer	444.05	450.33	894.38	50.35	5.71	44.64
All Oligomers	23938.12	6172.74	30110.86	20.50	0.43	20.07
	DPP2					
	Avg .Unbound Signal	*Avg. Bound Signal*	*Total Signal for Bound/Unbound*	*% Bound*	*% ThT Bound*	*Normalized % Bound*
Monomer	4386.14	230.22	4616.37	4.89	0.26	4.63
Dimer	929.44	251.82	1181.26	20.37	0.00	20.37
Trimer	520.65	238.58	759.23	29.71	5.71	24.00
All Oligomers	5836.23	720.63	6556.86	10.60	0.43	10.18

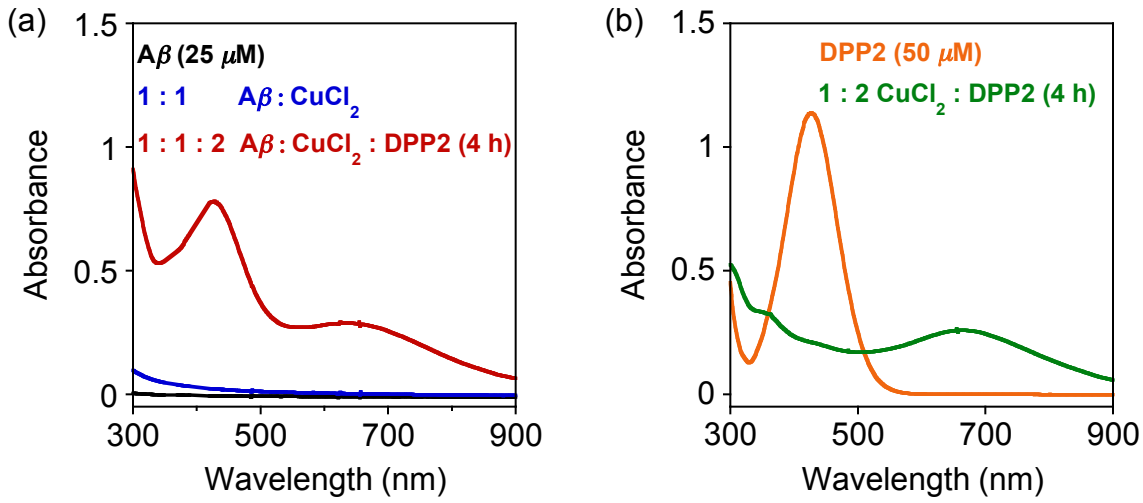

Figure A.1. Metal binding studies of **DPP2** in the absence and presence of Aβ at pH 6.6. (a) UV-Vis spectra of Aβ (black), Aβ + $CuCl_2$ (blue), and Aβ + $CuCl_2$ + **DPP2** (1:1:2 ratio, 4 h incubation; red). (b) UV-Vis spectra of **DPP2** without (orange) and with $CuCl_2$ (green). Conditions: [Aβ] = 25 μM; [$CuCl_2$] = 25 μM; [**DPP2**] = 50 μM; 20 mM HEPES, pH 6.6, 150 mM NaCl; room temperature.

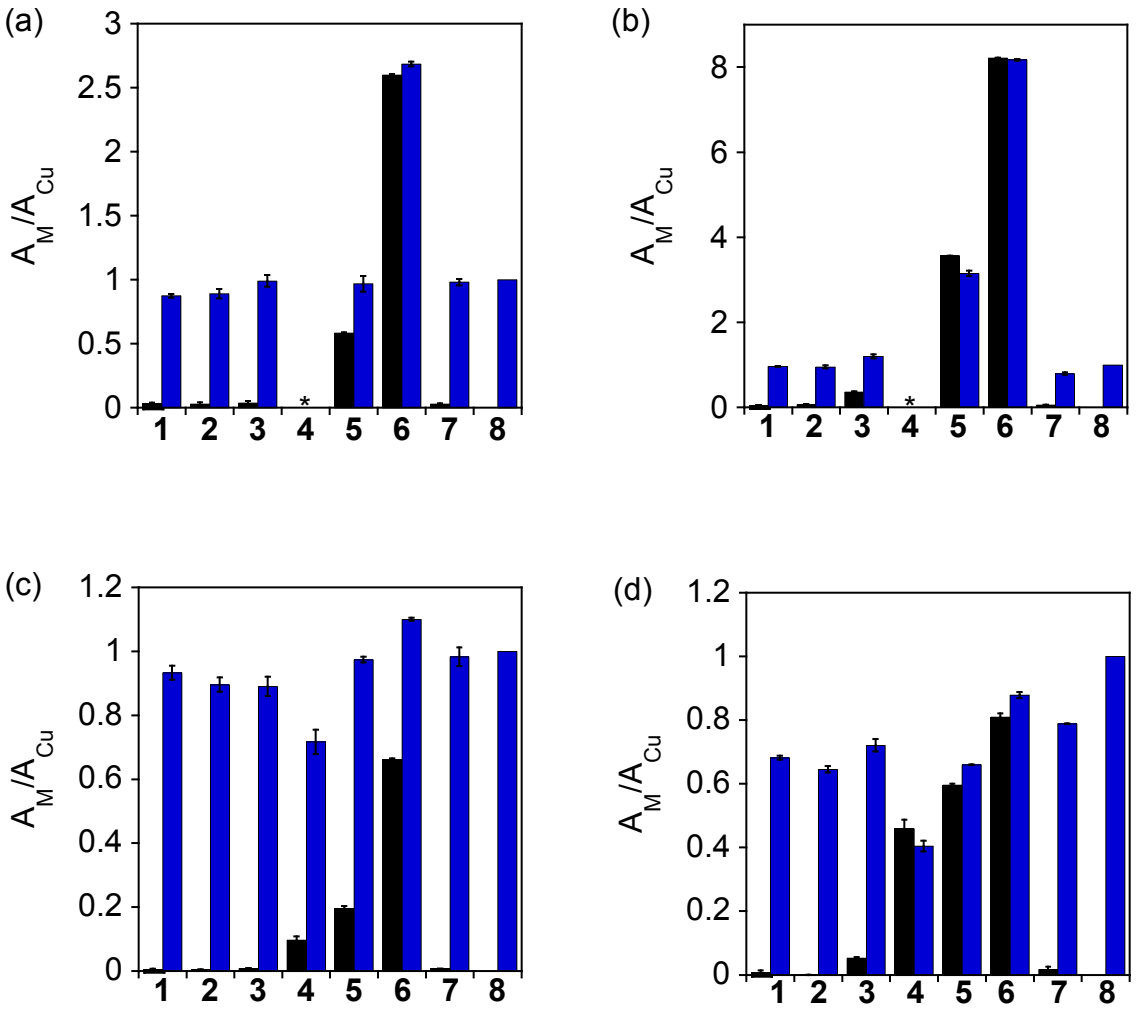

Figure A.2. Metal selectivity studies of **DPP1** (a and b; 40 μM) and **DPP2** (c and d; 20 μM) in EtOH. Blue bars represent the addition of $CuCl_2$ (**8**) to solutions of the ligand with other divalent metal ions (black bars; **1**: $MgCl_2$; **2**: $CaCl_2$; **3**: $MnCl_2$; **4**: $FeCl_2$; **5**: $CoCl_2$; **6**: $NiCl_2$; **7**: $ZnCl_2$) in a ratio of 1:1 (a and c) or 1:25 (b and d) Cu^{2+} to M^{2+} followed by 5 min incubation at room temperature. The absorbance at 360 nm (for **DPP1**) and 580 nm (for **DPP2**) was used for the calculation of A_M/A_{Cu}. * Precipitation was observed in the solution.

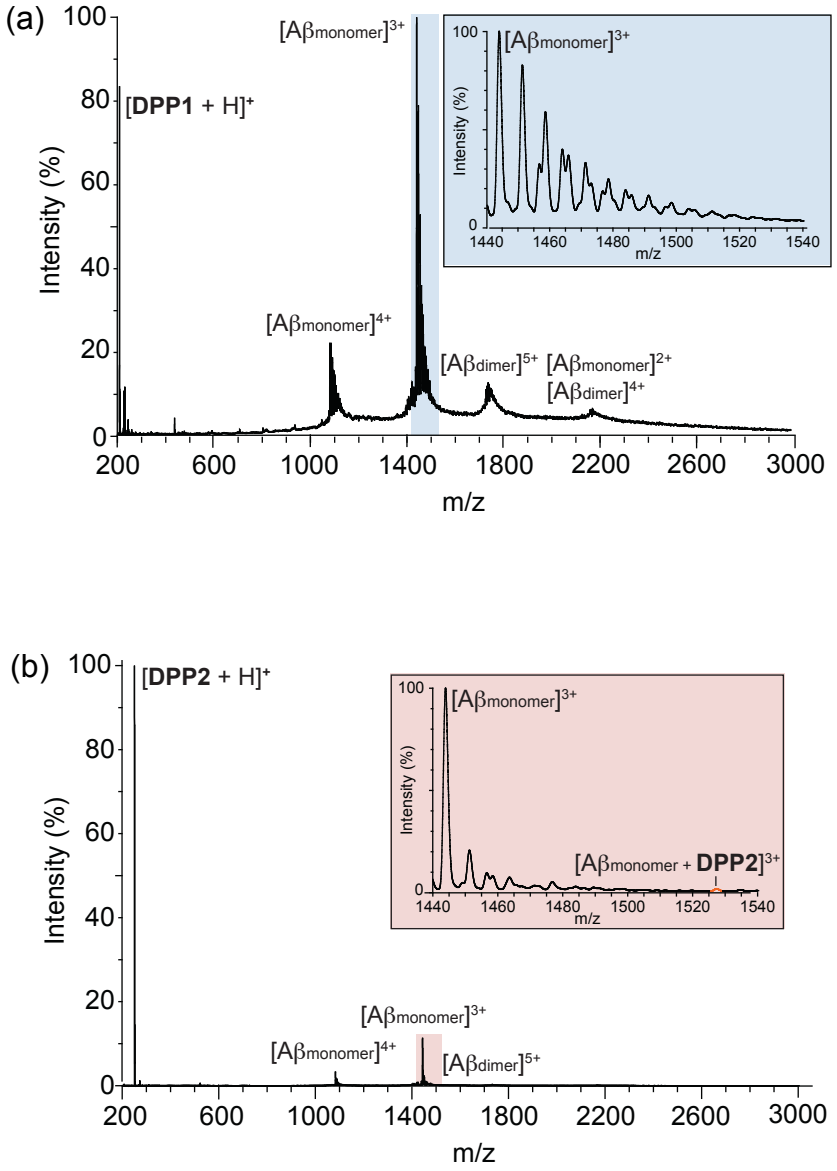

Figure A.3. Interaction of (a) **DPP1** (60 μM) and (b) **DPP2** (30 μM) with A$\beta_{1\text{-}40}$ (10 μM) determined by nano-electrospray ionization-mass spectrometry (nESI-MS). Binding of **DPP2** to Aβ monomer was observed in a ratio of 3:1 in the 3+ charge state (incubation time = 2 h on ice).

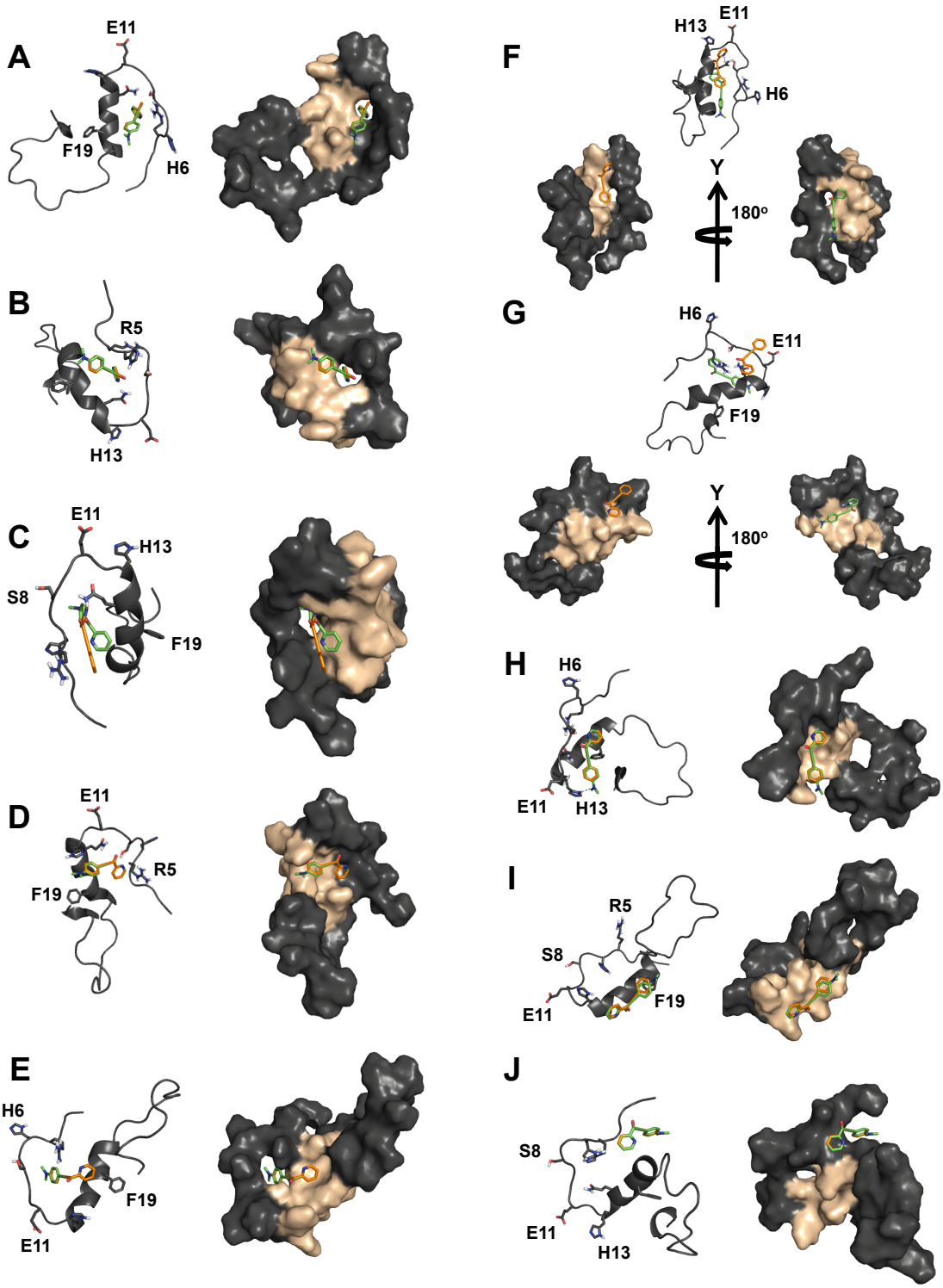
A
E11
F19
H6
B
R5
H13
C
E11
H13
S8
F19
D
E11
F19
R5
E
H6
F19
E11
F
H13
E11
H6
Y
180°
G
H6
E11
F19
Y
180°
H
H6
E11
H13
I
R5
S8
E11
F19
J
S8
E11
H13

Conformation	DPP1 (kcal/mol)	DPP2 (kcal/mol)
A	-6.3	-6.5
B	-6.1	-6.1
C	-5.6	-5.8
D	-5.5	-5.7
E	-5.6	-5.7
F	-5.9	-5.5
G	-5.4	-5.5
H	-5.4	-5.3
I	-5.4	-5.3
J	-5.2	-5.3

Figure A.4. Docking studies of **DPP1** and **DPP2**. Cartoon (left) and surface (right) versions of possible conformations of **DPP1** (orange) and **DPP 2** (green) docked with A$\beta_{1\text{-}40}$ (PDB 2LFM) by AutoDock Vina. The helical region of Aβ (H13 - D23) in the surface representation is highlighted in color (tan) and hydrogen bonding is indicated with dashed lines (2.5 - 2.8 Å) Conformation A is also depicted in Figure 2.3d. **Bottom**: Calculated binding energies of **DPP1** and **DPP2** to Aβ.

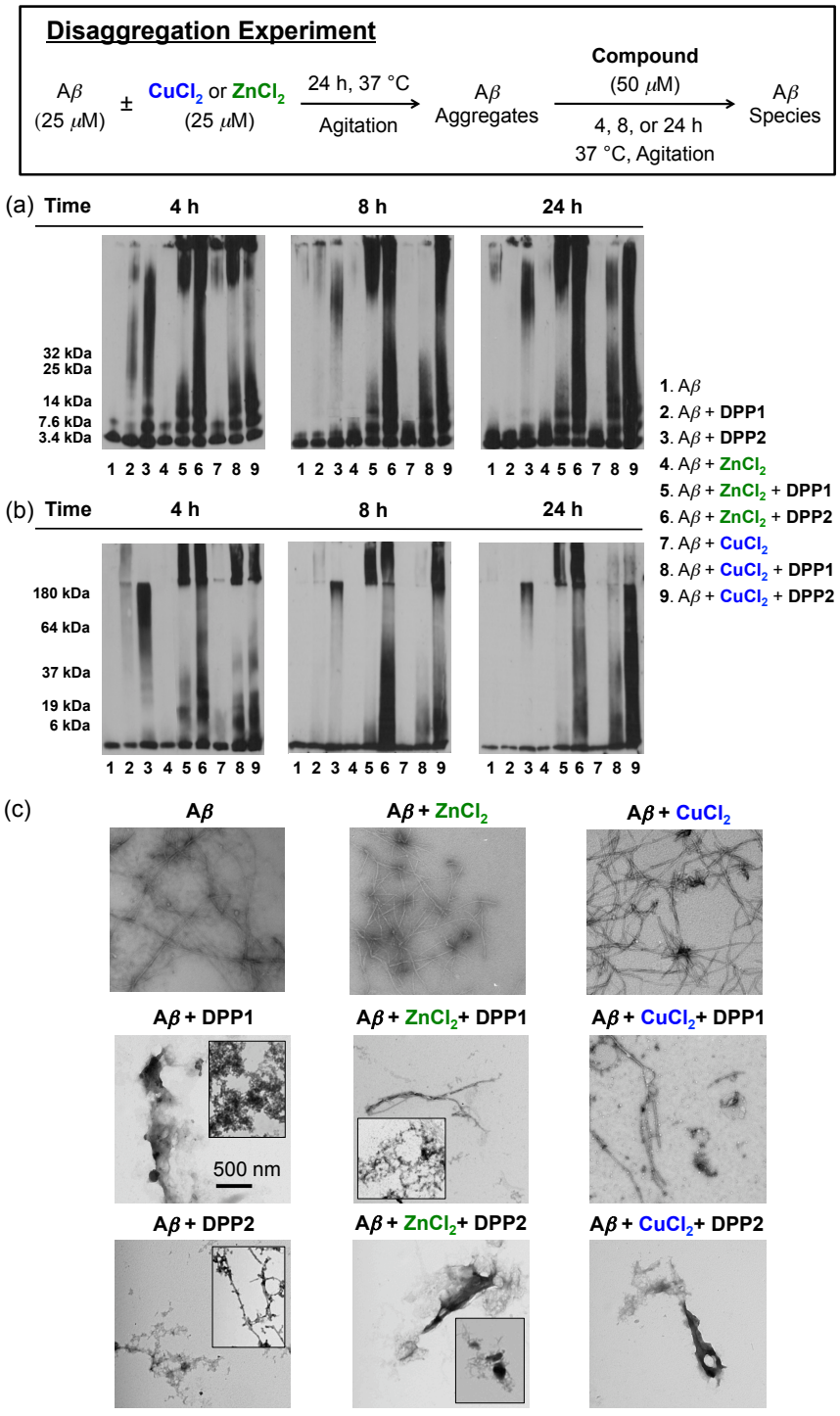

Figure A.5. Disaggregation experiment (scheme, **top**). Analysis of various-sized A*b* species by (a) native gel electrophoresis and (b) SDS-PAGE (non-reducing conditions) with Western blot (6E10). (c) TEM images of the 24 h incubated samples. Conditions: [A*b*] = 25 μM; [$CuCl_2$ or

$ZnCl_2$] = 25 μM; [compound] = 50 μM; pH 6.6 (for Cu^{2+} samples) or 7.4 (for metal-free and Zn^{2+} samples); 4, 8, or 24 h incubation; 37 °C; constant agitation.

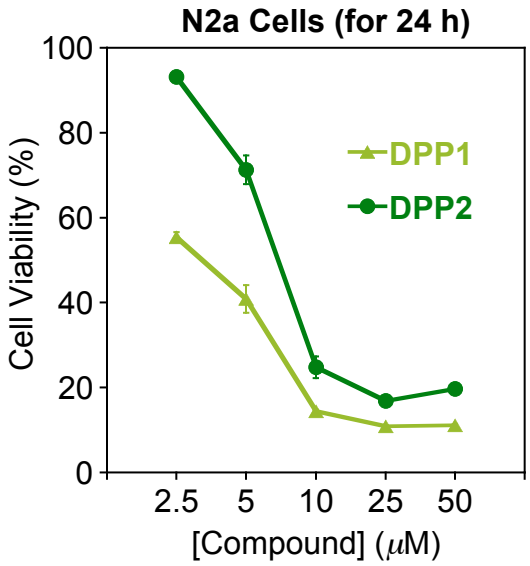

Figure A.6. Cytotoxicity of **DPP1** and **DPP2** at various concentrations (24 h incubation) in murine N2a neuroblastoma cells, which was determined by a MTT assay. Values of cell viabilitity (%) were calculated relative to cells treated with 1% v/v DMSO.

Appendix B. Supporting Information for Chapter 3

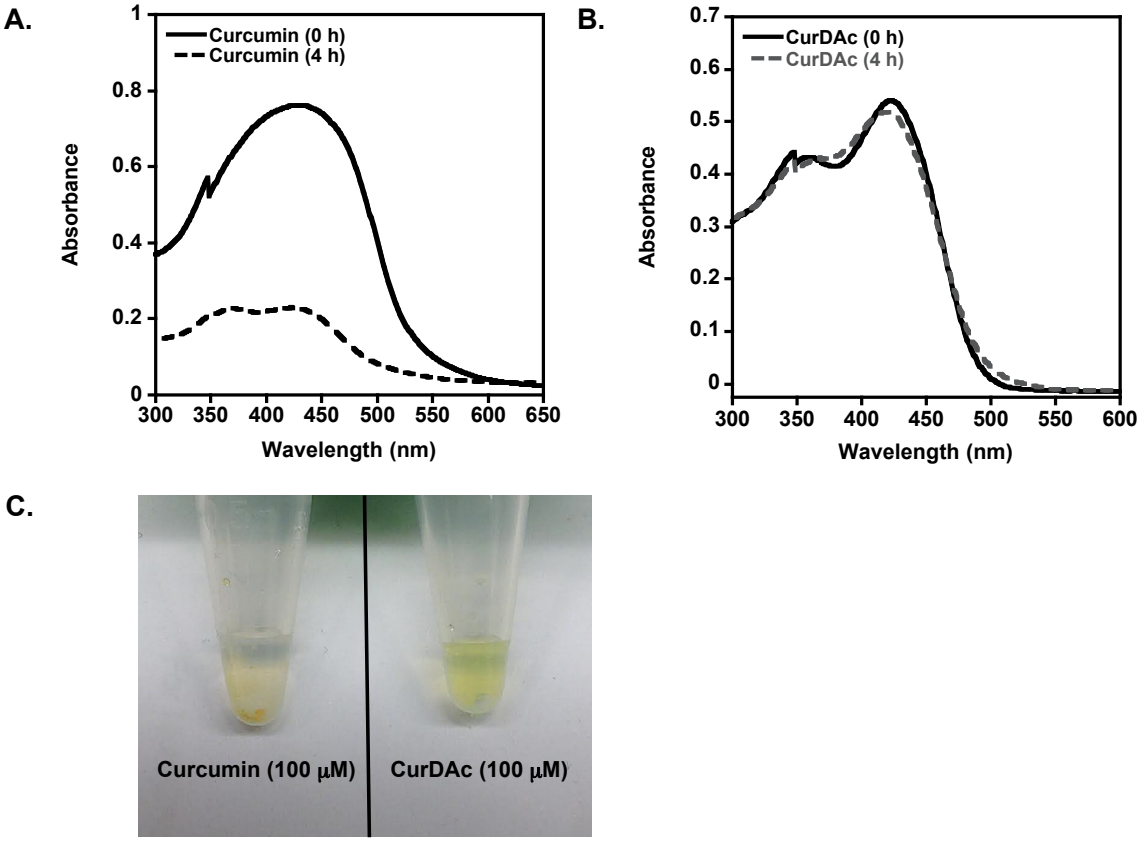

Figure B.1. UV-Vis spectra of A) curcumin and B) **CurDAc** (right). C) 100 mM curcumin (left) and 100 mM **CurDAc** (right). A solid pellet is formed from insoluble curcumin in water after centrifugation. Under identical conditions, **CurDAc** remains as a homogenous solution.

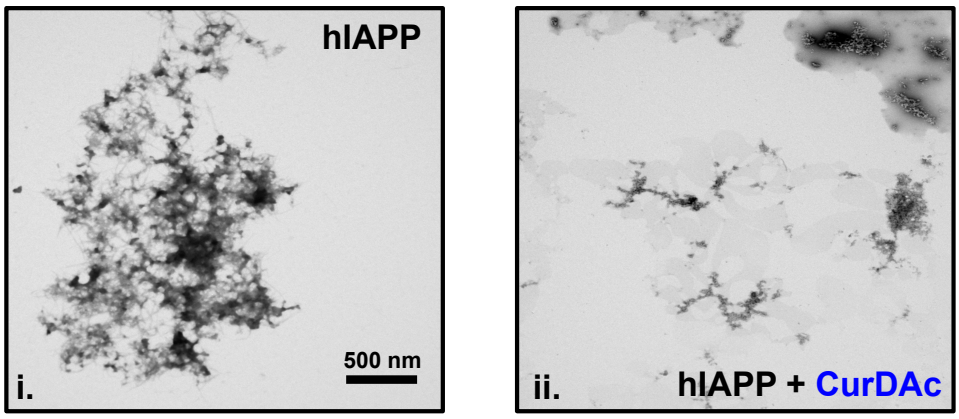

Figure B.2. Transmission electron micrographs of hIAPP (10 mM) alone (i) and incubated with **CurDAc** (ii). Samples visualized after 4 h. Upon incubation with **CurDAc** (10 mM), smaller, more amorphous hIAPP species are visible by TEM, unlike the fibril network seen with peptide alone.

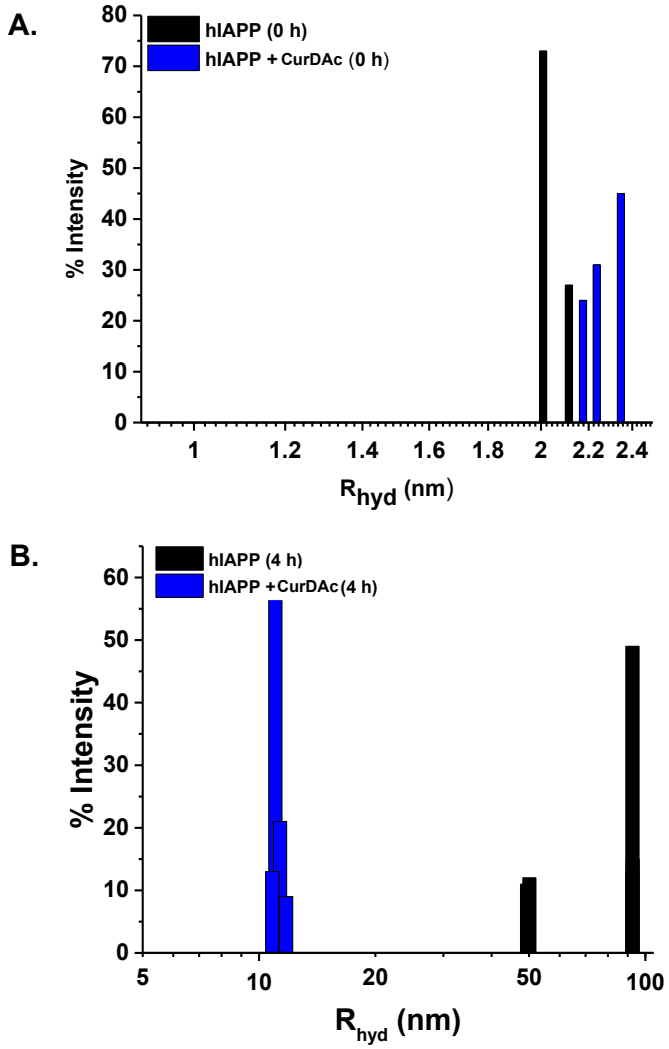

Figure B.3. Dynamic light scattering (DLS) graphs representing hydrodynamic radius (r_H) of hIAPP (black, 25 μM) and hIAPP with **CurDAc** (blue, 25 μM) at 0 h (a) and 4 h (b). Possible small hIAPP oligomer assemblies (r_H = 10 nm) are detected by DLS in the presence of **CurDAc** whereas larger oligomeric or protofibrillar aggregates are seen for peptide alone after 4 h.

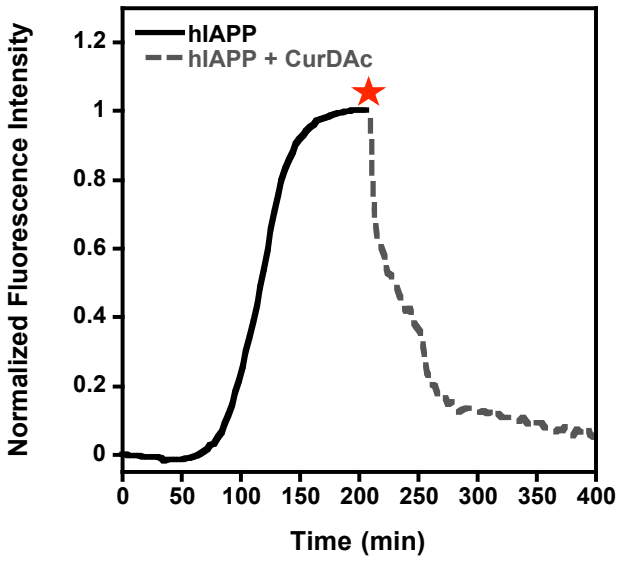

Figure B.4. ThT assay used to measure the disaggregation of preformed hIAPP (10 μM, black) fibers with **CurDAc** (10 μM, grey). The red star indicates the time when **CurDAc** was added. As discussed in the main text, these results indicate that **CurDAc** can depolymerize preformed hIAPP fibrils in solution over time.

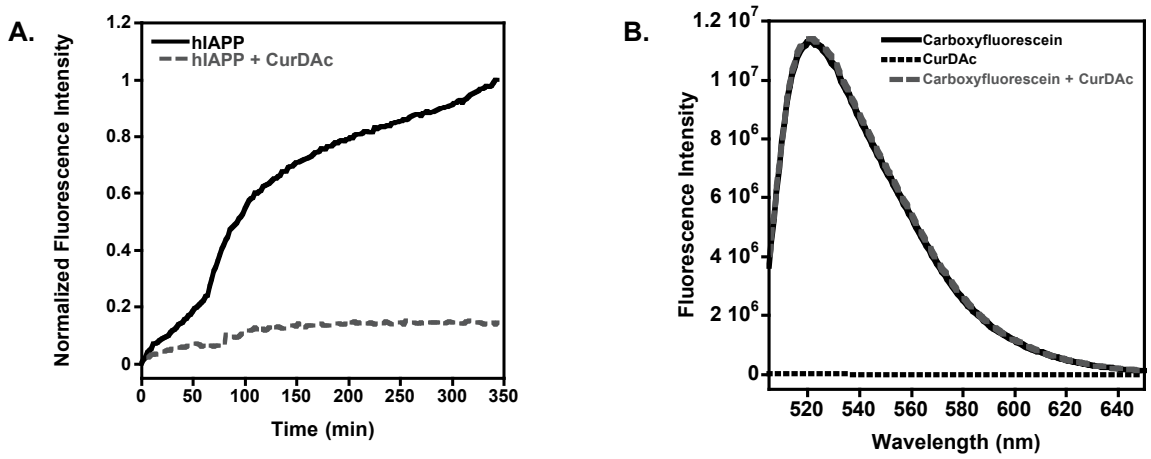

Figure B.5. Dye leakage assay of POPC:POPG (7:3) LUVs (0.2 mg/mL) encapsulated with 6-carboxyfluorescein. hIAPP alone (black, 10 μM) shows an increase in dye release which is mitigated when **CurDAc** is present (grey, 10 μM). There is no overlap in the fluorescence signal when **CurDAc** is present (B) indicating no interference from the small molecule.

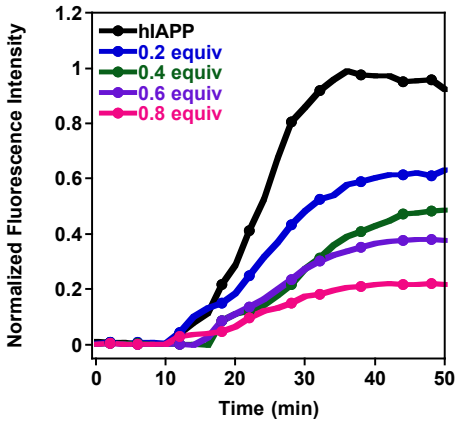

Figure B.6. Concentration dependent inhibition of hIAPP (10 μM) with CurDAc. As the equivalence of **CurDAc** is increased, a greater inhibitory activity is observed.

Appendix C. Supporting Information for Chapter 4

Table C.1:. Mdp-Parameters for Reconstruction Simulation.

Parameter	Values
Initialcapping force $F_{cap},0$	15,000kJmol^{-1}nm^{-1}
Capping increase rate A	100kJmol^{-1}nm^{-1}ps^{-1}
Restraining force constant k	12,000kJmol^{-}1nm^{-2}
Radius of CG water r_{CGW}	0.21nm
Water restraining force constant k_W	400kJmol^{-1}nm^{-2}
Nr of steps to release restraints	5000
Annealing method	single
Annealing time	60ps
Initial annealing temperature	1300K

Table C.2. A Summary of Structural Statistics for the 20 Final NMR Structures of TK9.

Distance restrains	TK9
Intra-residue (i–j = 0)	26
Sequential (|i–j| = 1)	21
Medium-range (2≤|i–j|≤4)	0
Long-range (|i–j| ≥5)	0
Total	47
Angular restraints	
Φ	8
Ψ	8
Distance restraints from violations (≥ 0.3Å)	0
Deviation from mean structure (A°) Average back bone to mean structure	1.69 ± 0.22
Average heavy atom to mean structure	3.43 ± 0.40
Ramachandran plot for mean structure	
% Residues in the most favourable and additionally allowed regions	100
% Residues in the generously allowed Region	0
% Residues in the disallowed region	0

Table C.3. Secondary structure distribution among the assembled and scattered peptides

Assembled 135 residues (15 chains)	**Scattered 45 residues (5 chains)**
60% residues are in the form of turns	64% residues are in the form of turns
36.29% residues are in the form of coils	28% residues are in the form of coils
3.70% are in the form of pi helix	6.67% residues are in the form of 3_{10} helix

Table C.4. Salt bridge interactions

Residue Pairs	**Average Distance (nm) Salt bridge interaction**
THR-1:LYS-9	2.174
ARG-7:LYS-9	2.310
LYS-9:LYS-9	2.433

Table C.5. Cation-Pi (π) Interactions within 6 Å

Residue Pair	Distance [cation-Pi (π)]	Angle	Count
TYR-3:ARG-7	5.28	48.66	1
TYR-5:ARG-7	5.40	135.44	2
TYR-5:ARG-7	5.71	133.85	
TYR-5:LYS-9	5.33	140.66	3
TYR-5:LYS-9	5.37	162.77	
TYR-5:LYS-9	5.92	117.99	

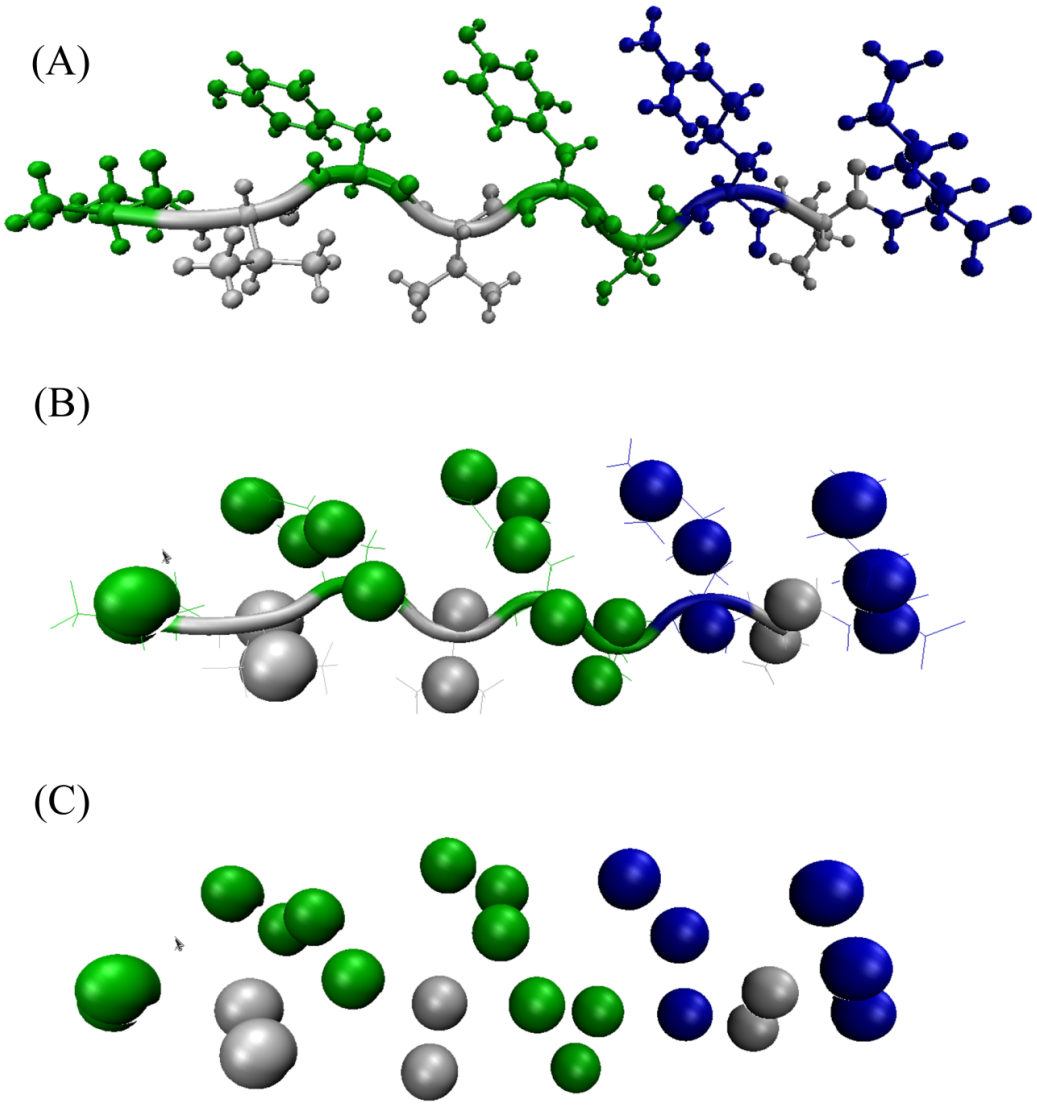

Figure C.1. (A) Extended conformation of TK9 obtained from solution NMR experiments; (B) Superimposition of coarse grained model and all atom model of a monomer; (C) Coarse grained model of monomer in the form of 24 beads based on MARTINI force fields.

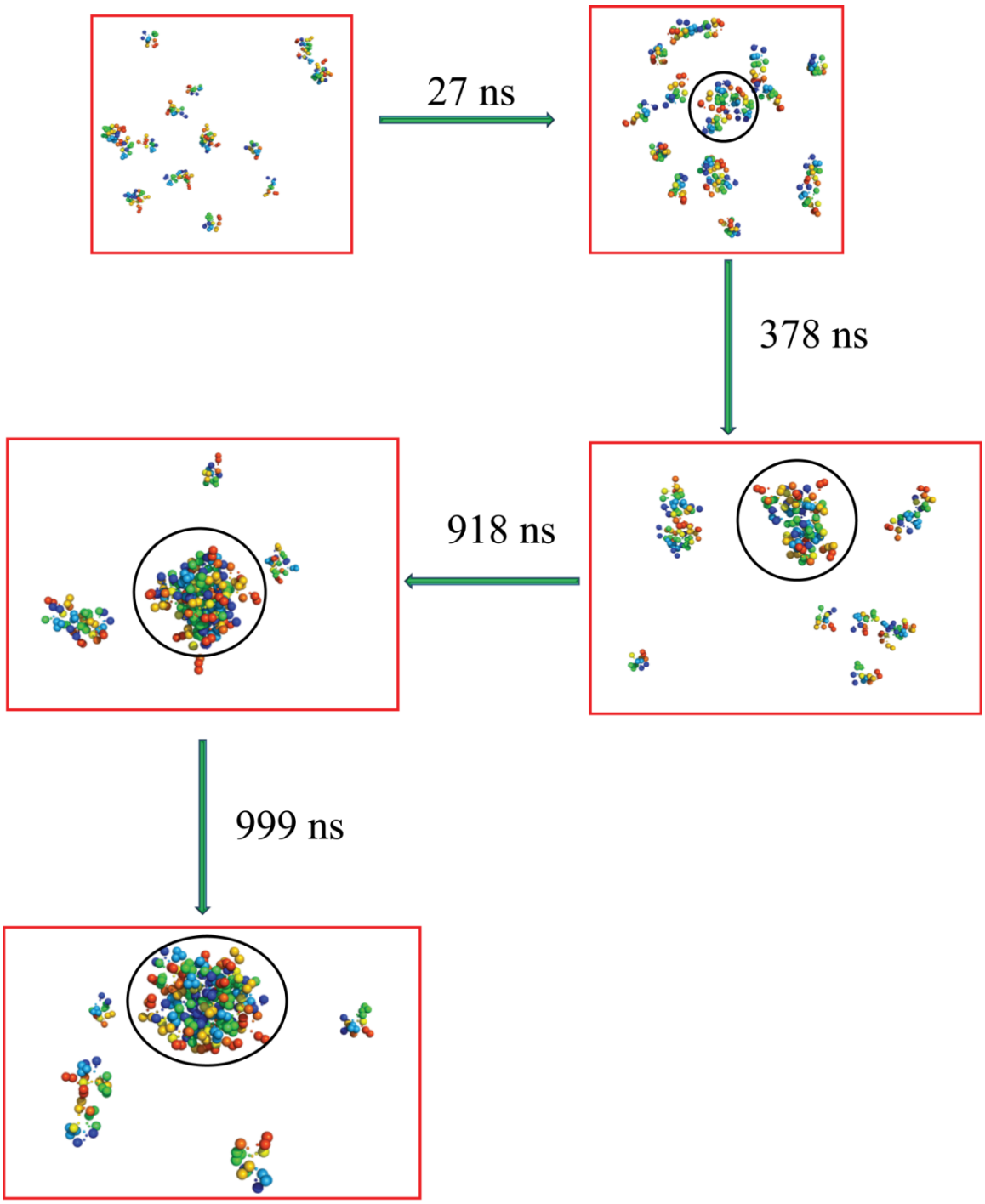

Figure C.2. Self-assembly of peptides from scattered to clustered form, structures captured at different time steps.

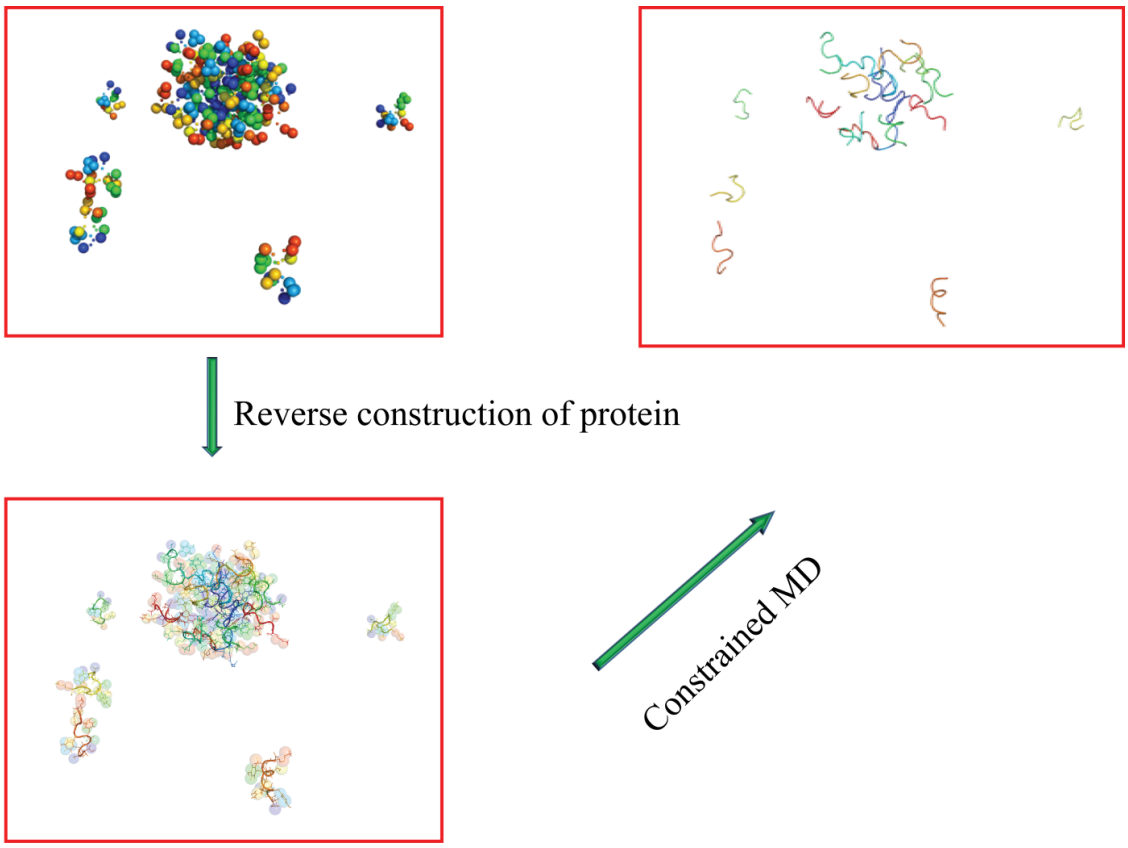

Figure C.3. Reconstruction of all atom system from coarse-grained model.

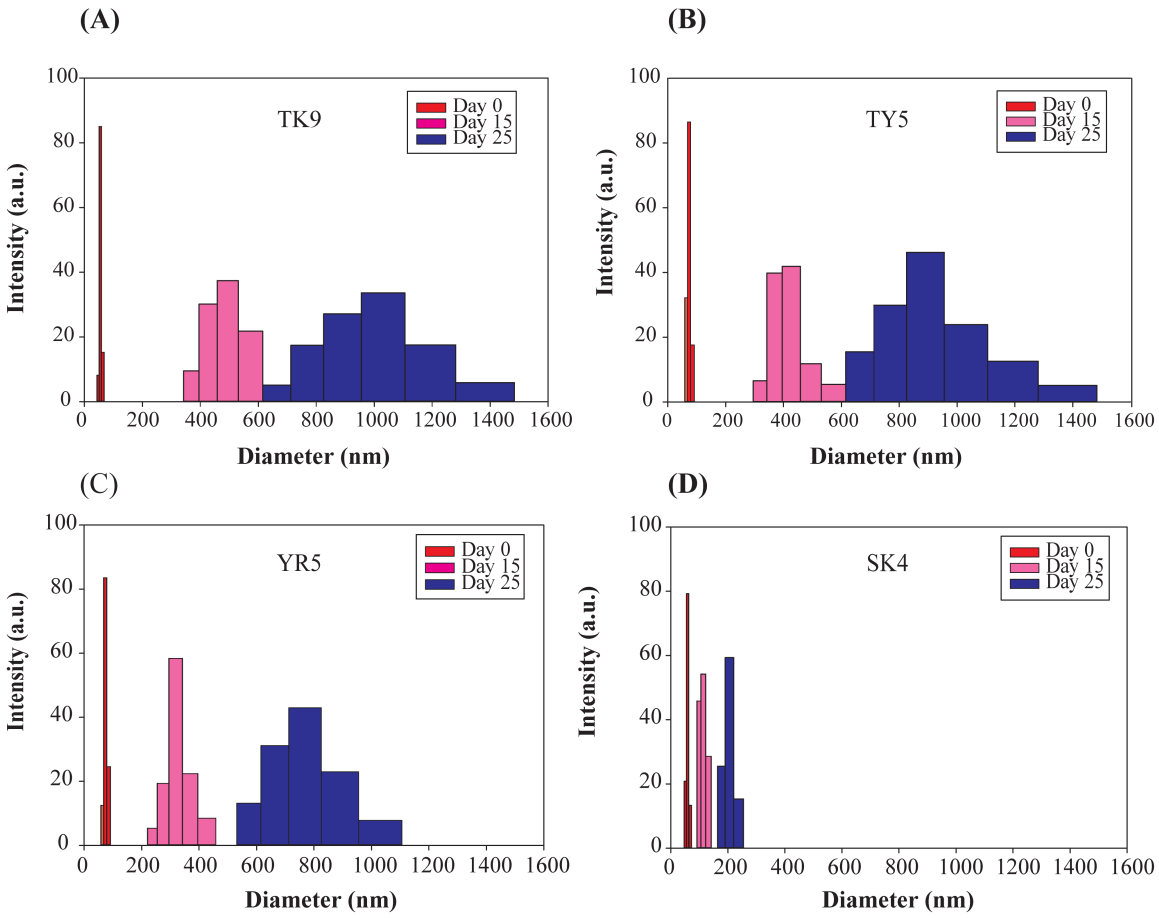

Figure C.4. Dynamic light scattering (DLS) data for TK9 (A) and its fragments TY5 (B), YR5 (C) and SK4 (D) showing extent of aggregation. The intensity vs. size distribution bar diagram are plotted at different time intervals.

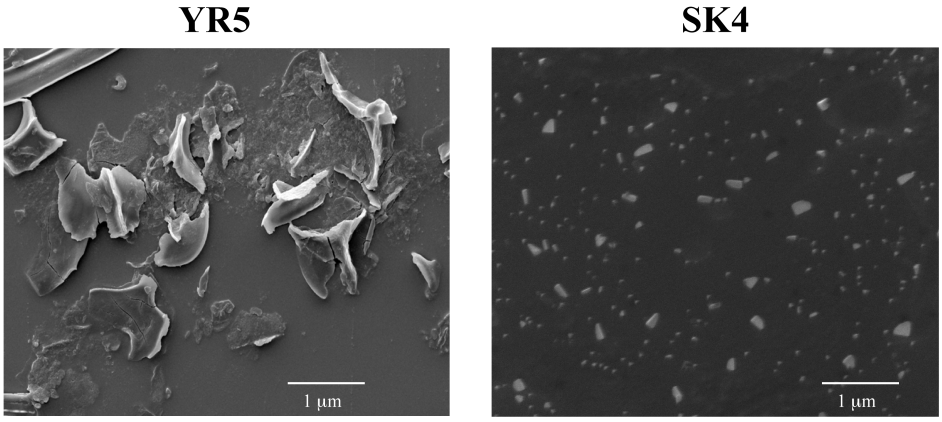

Figure C.5. Scanning electron micrograph of YR5 and SK4 sample after 25 days of incubation.

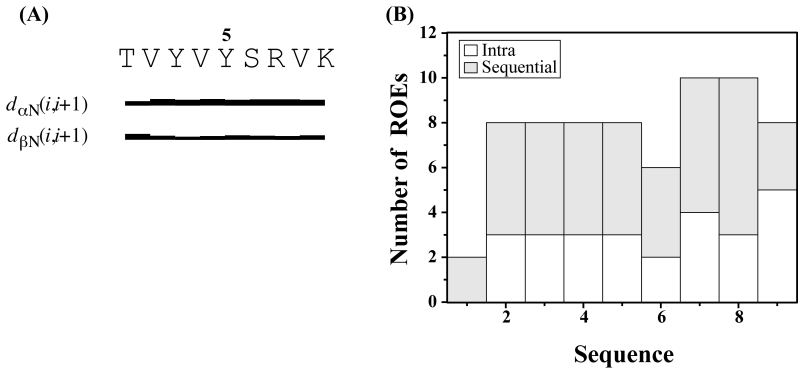

Figure C.6. (A) Bar diagram summarizing type (sequential, medium range, and long range) and number of ROE contacts, in the ROESY spectra of TK9. The thickness of the bars indicates the intensity of the ROESY peaks, which are assigned as strong, medium, and weak. The primary amino acid sequences of each peptide are shown at the top. (B) A histogram showing the number and type (intra, sequential, medium) of ROEs of TK9 as a function of residue number.

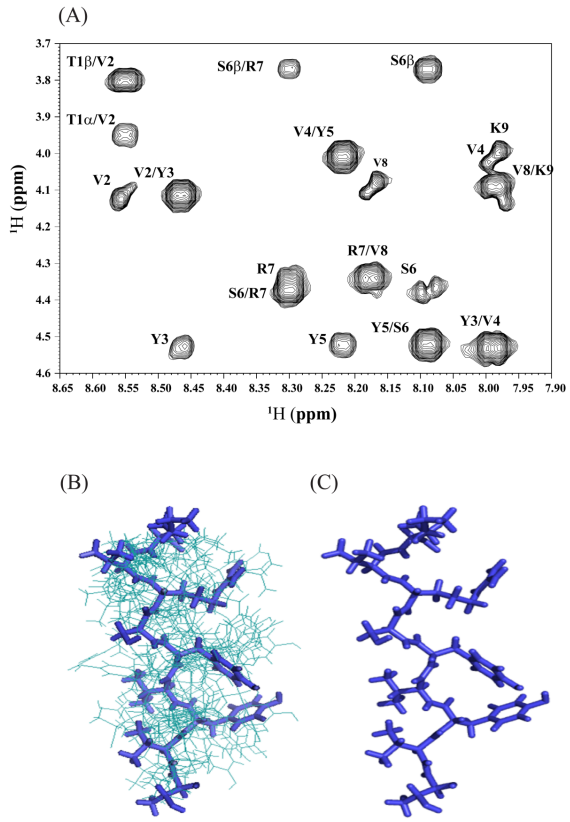

Figure C.7. (A) Two-dimensional ^{1}H/^{1}H ROESY spectrum of TK9 in aqueous solution. (B) ROE derived 20-ensemble structures of TK9. (C) Average structure of TK9.